Volume 11
Number 21
7 June 2023
Pages 6765–7108

# Journal of Materials Chemistry C

Materials for optical, magnetic and electronic devices

rsc.li/materials-c

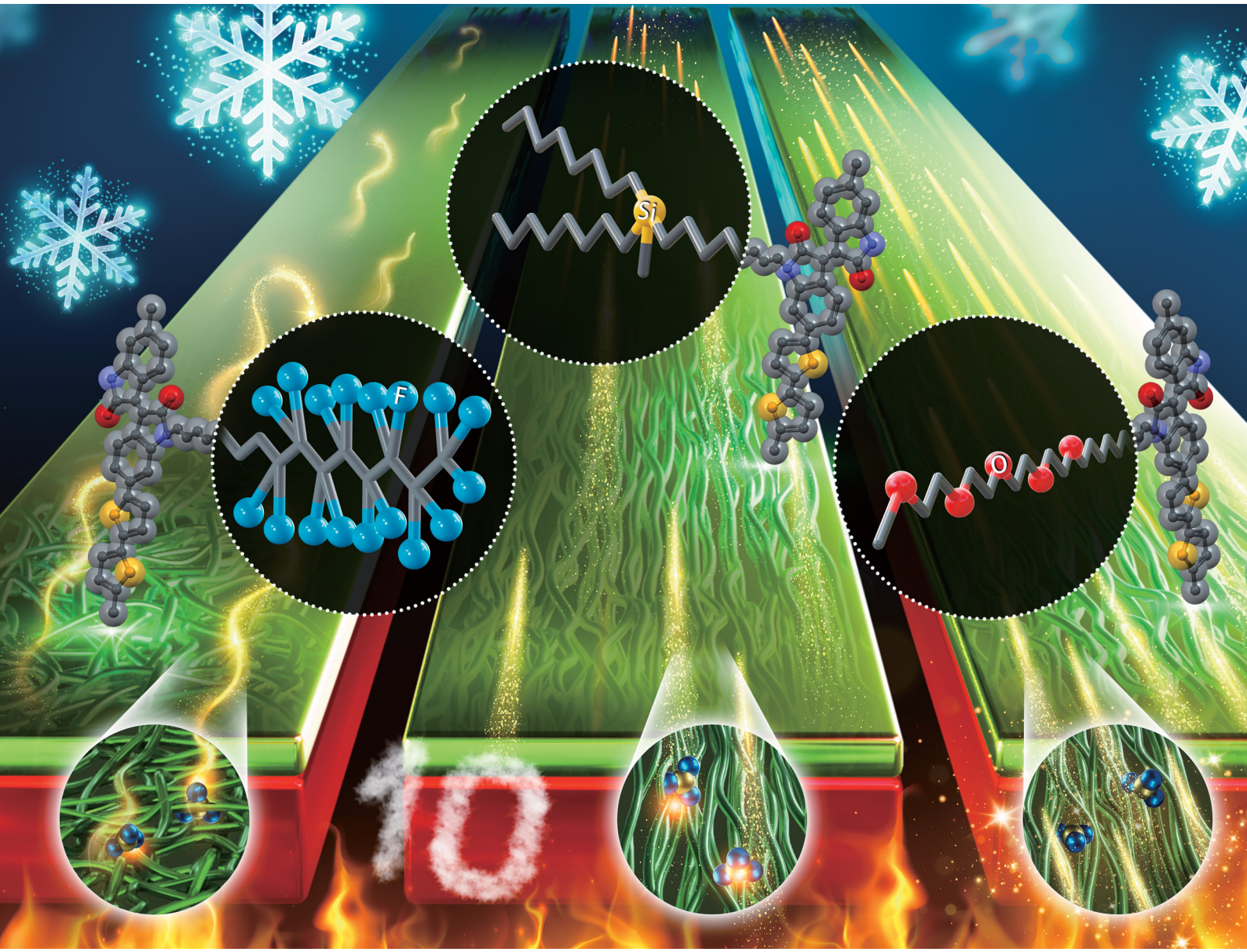


ISSN 2050-7526

ROYAL SOCIETY OF CHEMISTRY

**PAPER**

Yan-Cheng Lin, Cheng-Liang Liu *et al.*
Optimizing the doping efficiency and thermoelectric properties of isoindigo-based conjugated polymers using side chain engineering

10 YEARS ANNIVERSARY

Journal of Materials Chemistry C

ROYAL SOCIETY OF CHEMISTRY

PAPER

View Article Online
View Journal | View Issue



Cite this: J. Mater. Chem. C, 2023, 11, 6874

# Optimizing the doping efficiency and thermoelectric properties of isoindigo-based conjugated polymers using side chain engineering†

Chia-Hao Tsai,[a] Yan-Cheng Lin, *[bc] Wei-Ni Wu,[a] Shih-Hung Tung, [cd] Wen-Chang Chen [ce] and Cheng-Liang Liu *[ac]

Received 10th March 2023,
Accepted 15th April 2023

DOI: 10.1039/d3tc00883e

rsc.li/materials-c

The chemical design of side chains and the physical control of molecular aggregation on conjugated polymer semiconductors have been demonstrated to be effective strategies for achieving efficient doping and charge transport in preparing doped conjugated polymer thermoelectric devices. Herein, our study introduces a unique approach for regulating the doping efficiencies and the thermoelectric properties of polymers, which involves manipulating the hydrophilicity and asymmetric side chain engineering. From isoindigo–bithiophene (IID–T2) donor–acceptor conjugated polymers, three polymers named **P(Si–Si)**, **P(Si–O)**, and **P(Si–F)** with the symmetric carbosilane side chains, asymmetric carbosilane/oligoether, and carbosilane/semifluorinated side chains, respectively, attached on the IID rings are investigated for their $FeCl_3$-doped thermoelectric films. It is found that the morphological structures and molecular packing can be controlled by altering the hydrophilicity and asymmetricity of side chain substituents. The doped **P(Si–O)** from the asymmetric side chain with oligoether moieties exhibits the maximum power factor of 23.4 μW $m^{-1}$ $K^{-2}$, which is attributed to the high doping efficiency of the polymers due to the intercalation of dopant molecules in the polymer side chains (without chain orientation disruption) while maintaining the charge transport percolation morphologies. The poor affinity between the semifluorinated side chains in **P(Si–F)** and dopants results in aggregation morphologies with low thermoelectric performance. These findings suggest that the combined asymmetric and hydrophilic side chains in conjugated polymers can effectively facilitate their miscibility with dopants for improving thermoelectric properties.



## 1. Introduction

Driven by the energy crisis and accelerating industrial and population growth, many researchers are searching for alternative energy sources and focusing on materials that contribute to energy conservation to meet energy demands.[1–3] Thermoelectric materials are one of the promising revolutions for realizing this goal since they can directly convert waste heat into electrical energy, enabling the energy harvesting of low-grade energy.[4,5] Generally, the energy-conversion efficiency of thermoelectric materials is determined by the figure of merit, $ZT$, which is expressed by the equation of $ZT = S^2\sigma T/\kappa$, where $S$ is the Seebeck coefficient, $\sigma$ is the electric conductivity, $\kappa$ is the thermal conductivity, and $T$ is the absolute temperature.[6,7] Since organic materials intrinsically possess ultralow $\kappa$, the power factor (PF = $\sigma S^2$) is thereby an index utilized to simplify the evaluation of thermoelectric properties of organic-based materials. The creation of materials with high $\sigma$ and $S$ and low $\kappa$ is crucial for thermoelectric research. Over the past decades, organic-based thermoelectric materials have offered the potential for obtaining high thermoelectric performance, especially at low temperatures, owing to their unique features of molecularly designed properties that can be fine-tuned, facile solution processability for scalable manufacturing, low cost of earth-abundant materials and production facilities, and suitability for flexible/wearable applications. In recent years, there has been a focused effort towards the study of numerous conducting polymers, such as polyaniline (PANI), polypyrrole (PPy),

[a] Department of Materials Science and Engineering, National Taiwan University, Taipei 10617, Taiwan. E-mail: liucl@ntu.edu.tw
[b] Department of Chemical Engineering, National Cheng Kung University, Tainan 70101, Taiwan. E-mail: ycl@gs.ncku.edu.tw
[c] Advanced Research Center of Green Materials Science and Technology, National Taiwan University, Taipei 10617, Taiwan
[d] Institute of Polymer Science and Engineering, National Taiwan University, Taipei 10617, Taiwan
[e] Department of Chemical Engineering, National Taiwan University, National Taiwan University, Taipei 10617, Taiwan

† Electronic supplementary information (ESI) available. See DOI: https://doi.org/10.1039/d3tc00883e

poly(3-hexylthiophene) (P3HT), and poly(3,4-ethylenedioxythiophene)poly(styrenesulfonate) (PEDOT:PSS), with the aim of achieving enhanced thermoelectric properties. This can be achieved through various methods such as doping or post-treatment. Additionally, these polymers have the advantage of inherent flexibility, making them attractive for use in flexible devices. Furthermore, if these materials can exhibit improved thermoelectric performance, it is expected to contribute significantly to the development of thermoelectric coolers. Therefore, considerable research efforts have been devoted to investigating the thermoelectric properties of these polymers, with the goal of improving their performance and developing new applications.[8–25]

Inherently conjugated polymers exhibit relatively low $\sigma$, and chemical doping, which occurs alongside the charge transfer between the host polymer and dopant molecules, is indispensable for increasing the carrier concentration in doped polymer films. The dopants (usually $FeCl_3$[26–41] and 7,7,8,8-tetracyanoquinodimethane (TCNQ)[42–54] derivatives used for p-doping) tend to aggregate from phase separation, and the charge transport of the pristine polymers is interrupted, resulting in a low $\sigma$ and thus low PF value. Consequently, the doping efficiency ($\eta_d$) significantly depends on the miscibility between polymer and dopant as well as their corresponding microstructures.[55,56] The complex molecular design of conjugated polymers and their blend morphologies with dopants are crucial in determining the final thermoelectric performance. The π-conjugated donor–acceptor copolymers with strong intramolecular interaction between donor and acceptor moieties can effectively extend π-conjugation while enhancing charge transport ability in the main chain and interchain π-stacking, which has been used for improving thermoelectric performance.[32,40] Additionally, there is still much room for improving the thermoelectric properties of donor–acceptor conjugated polymers *via* side chain engineering, which significantly impacts the molecular crystallization, polymer/dopant miscibility, and blend morphologies in the active thermoelectric layer.[26–31,42,43,57–59] The addition of glycol side chains to donor–acceptor polymers can ensure the dispersion of dopants in the polar environment of the glycol chain rather than the nonpolar alkyl chain, resulting in improved $\eta_d$ and $\sigma$.[36,44–48,60–69] Furthermore, Yoon *et al.* designed a series of IID-based copolymers with alkyl chains of different lengths for $FeCl_3$-doped thermoelectric films. They found that increasing the proportion of amorphous regions with bulky alkyl chains promotes efficient molecular doping of polymers while preserving high mobility from their planar backbone, leading to a PF increase of up to 37.8 μW m$^{-1}$ K$^{-2}$ from the $\sigma$ enhancement.[30] Based on the aforementioned discussion, the strategies motivate us to believe that in our previous work,[70] the combination of asymmetric and polar oligoether side chains in IID–T2 copolymers can cause a slight reduction in crystallinity without severely reducing the mobility. It is believed that donor–acceptor copolymers attached with asymmetric and oligoether side substituents potentially possess high miscibility between polymer and dopants, resulting in remarkably enhanced thermoelectric performance.

Our study aims to examine the effect of varying the molecular design of host conjugated polymers through asymmetric side chain substituents on the $\eta_d$ and thermoelectric properties of resulting $FeCl_3$-doped polymer films. To achieve this, three conjugated copolymers (based on IID–T2 as the main building backbones) were synthesized and compared: the first incorporates symmetric carbosilane groups on both side chains of IID moieties as a reference (**P(Si–Si)**), while the others feature asymmetric carbosilane/oligoether and carbosilane/semifluorinated side chains (**P(Si–O)** and **P(Si–F)**). The objective of this study is to investigate the relationship between polymer structure and thermoelectric performance by examining the modification of polymers using side chains of varying hydrophilicity. The study shows that using asymmetric side chains can increase the amorphous domains of the polymer, leading to improved doping efficiency. Consequently, incorporating the concept of asymmetric side chain engineering has a significant impact on the thermoelectric properties of the material. The $\eta_d$ of the three polymers was determined using UV-vis-NIR spectroscopy and X-ray photoelectron spectroscopy (XPS), while the electronic states upon doping were examined using ultraviolet photoelectron spectroscopy (UPS). The morphological and microstructural properties of pristine and doped polymer films were characterized by atomic force microscopy (AFM) and grazing-incidence wide-angle X-ray scattering (GIWAXS), respectively. The high $\sigma$ and $\eta_d$ of **P(Si–O)** resulted in a maximum PF of 23.4 μW m$^{-1}$ K$^{-2}$, which is two to six times higher than that of the other polymers. This was attributed to the high host-dopant miscibility from the introduction of the hydrophilic oligoether side chain of **P(Si–O)** as well as the high degree of structural ordering/crystallinity. Thus, we utilized the combined concepts from asymmetric and oligoether side chains for highly efficient p-doing of conjugated polymers with high thermoelectric performance.

## 2. Experimental section

### 2.1. Materials

Three isoindigo-based donor–acceptor conjugated polymers, **P(Si–Si)**, **P(Si–O)**, and **P(Si–F)**, were synthesized according to our previously reported procedures.[71] All the solvents and chemicals were purchased from commercial sources without further purification unless otherwise indicated.

### 2.2. Fabrication and measurement of thermoelectric devices

The glass substrates were cleaned by sonication in acetone, isopropanol, and deionized water for 10 min in each step, followed by oxygen plasma treatment for 10 min. Immediately after the plasma treatment, the conjugated polymer solution (10 mg mL$^{-1}$ in chlorobenzene) was spin-coated onto the substrate in a nitrogen-filled glove box and annealed at 200 °C for 60 min. The doping process was done by immersing the pristine polymer films into the 3 mg mL$^{-1}$ $FeCl_3$ solution in acetonitrile. After 3 min, the device was dried with a nitrogen flow. The thicknesses of doped conjugated polymer films were estimated by stylus profilometers and found to be ~100 nm. Then these doped polymer film-coated substrates were cut into rectangular with dimensions of 7 × 15 mm, and both ends were coated with

silver paste for measurement contact. The thermoelectric parameters of doped polymer thin film samples, including Seebeck coefficient and electrical conductivity, were simultaneously measured by a commercial ZEM-3 measurement system (ADVANCE RIKO Inc., Japan) at 323 K under a helium atmosphere.

## 3. Results and discussion

### 3.1. Spectroscopic analysis

In a previous study, we found that combining asymmetric and hydrophilicity side chains is effective for achieving high-performance semiconducting polymer.[71] This side chain modification can also be applied to manipulate dopant/polymer miscibility while simultaneously maintaining desirable properties, such as microstructural organization and effective thermoelectric effect. The chemical structures of the three polymers with identical conjugated main chains but different symmetric (**P(Si–Si)**)/asymmetric (**P(Si–O)** and **P(Si–F)**) substitutions on the side chain were studied for thermoelectric application (Scheme 1). For the molecular weight, due to the asymmetric side chain design, **P(Si–O)** and **P(Si–F)** attain the molecular weight of 244 and 355 kDa, respectively, enabling them to demonstrate superior solubility, in contrast to the 80 kDa observed for **P(Si–Si)**. Besides, for the thermal properties, there appears to be no thermal transition within the temperature range of 50 to 250 °C, which are summarized in Table S1 (ESI†).[71] The UV-vis-NIR spectra of pristine and doped polymer films were measured to characterize the p-doping behaviors of IID-based copolymers, as shown in Fig. 1. The pristine polymers exhibited dual absorption regions at 300–500 and 500–800 nm, representing the π–π* transition of conjugated cores and intramolecular vibrational coupling, respectively.[72] Unlike **P(Si–Si)**, the asymmetric polar **P(Si–O)** and **P(Si–F)** exhibited a slight red-shifted absorption band when the single carbosilane side chain was replaced by oligoether and fluorinated chains. This is attributed to the stronger interaction of conjugated polymer backbone. Upon doping with $FeCl_3$, a sharp decrease in the neutral polymer signal centered around 710 nm and a broad polaronic transition in the range of 900–2000 nm distinctively appeared, indicating the presence of electronic charge carriers during the p-doping of the

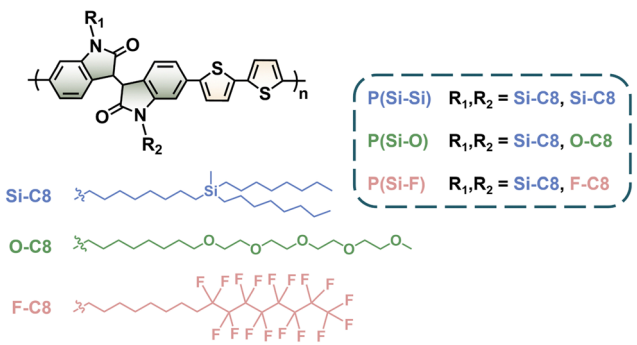


Scheme 1 Molecular structures of **P(Si–Si)**, **P(Si–O)**, and **P(Si–F)** reported in this work.

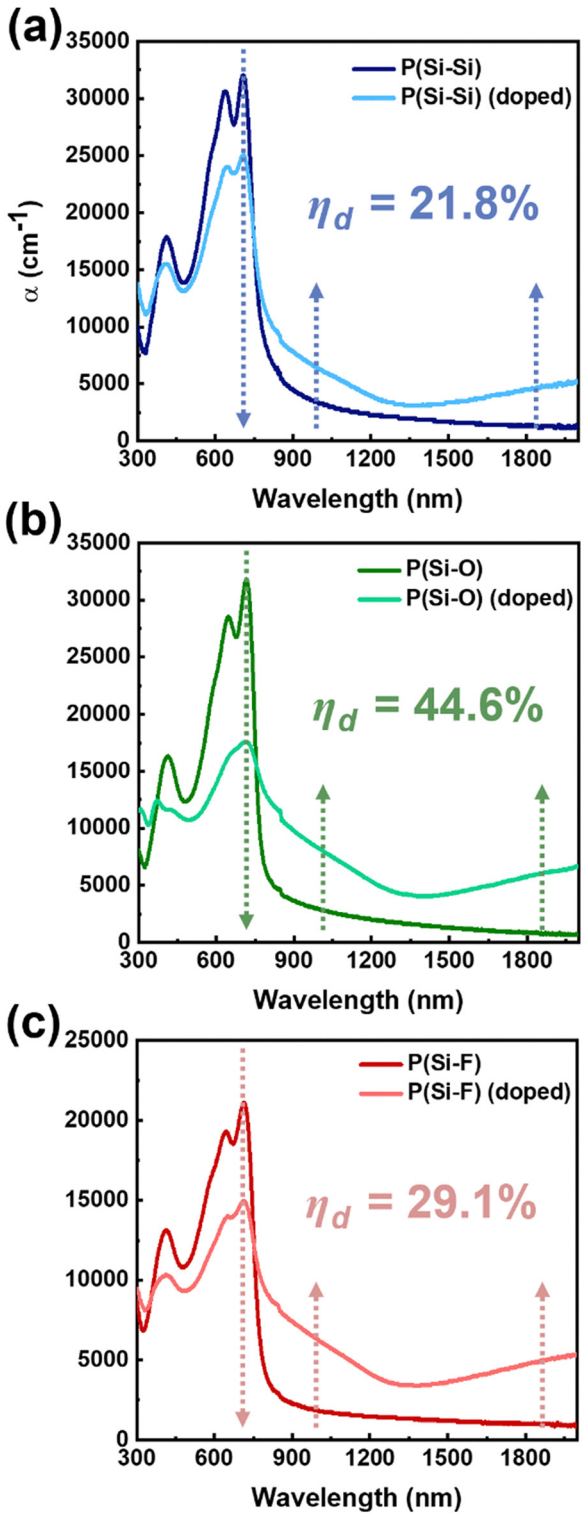


Fig. 1 UV-vis-NIR absorption spectra for undoped and $FeCl_3$-doped (a) **P(Si–Si)**, (b) **P(Si–O)**, and (c) **P(Si–F)** films.

polymers. **P(Si–O)** had a more pronounced optical transition upon doping with $FeCl_3$, indicating a more effective p-doping. The $\eta_d$ calculated from the decrease in the magnitude of the pristine polymer absorption peak at 708, 716, and 714 nm for

 

**P(Si–Si)**, **P(Si–O)**, and **P(Si–F)**, respectively, and the $\eta_d$ can be expressed as eqn (1):

$$\eta_d = \frac{I_o - I_d}{I_o} \quad (1)$$

where $I_o$ and $I_d$ are the intensity of the characteristic peak of pristine and doped polymer film, respectively. The calculated $\eta_d$ for **P(Si–Si)**, **P(Si–O)**, and **P(Si–F)** were 21.8%, 44.6%, and 29.1%, respectively.[36] Based on these calculations, the doping efficiency was found to be slightly higher for the asymmetric carbosilane/fluorinated side chain of **P(Si–F)** and significantly enhanced when the oligoether side chain was added to **P(Si–O)**, indicating a favorable interaction between the dopant and oligoether side chain of **P(Si–O)**.

In Fig. 2, UPS experiments were conducted on the film samples to assess the work functions and investigate the changes in electronic structures upon doping. After doping, a significant increase in the work function of all three polymer samples was observed, confirming the formation of a high concentration of polarons when the $FeCl_3$ dopants are thermodynamically capable of oxidizing the polymer. This result indicates a downshift in the Fermi level toward the highest occupied molecular orbital (HOMO) with effective hole transfer from the polymer to $FeCl_3$. Under the same doping conditions, the most distinct pinning at 0.66 eV above the transport level of **P(Si–O)** can be interpreted as the lowest thermal activation energy *via* integer charge transfer between the $FeCl_3$ dopant and **P(Si–O)**.[34] This implies that **P(Si–O)** is more likely to be doped by $FeCl_3$ and efficiently transfer carriers, reflecting a higher doping level than **P(Si–Si)** and **P(Si–F)**; this is consistent with the absorption results (Fig. 1).

Additionally, XPS measurements were conducted to detect the change in chemical components and electronic state of the three polymer films before/after doping with $FeCl_3$ (Fig. S1, ESI†). Additional Cl and Fe peaks in the range of binding energies of 196–202 eV and 705–740 eV were observed in the XPS results of the doped polymer films, which originate from the $FeCl_3$ dopants. When $FeCl_3$ is dissolved in a solvent, it dissociates into $FeCl_4^-$ and $FeCl_2^+$ ions. When these dopants are introduced into a polymer chain, the $FeCl_2^+$ ions can react with the polymer, leading to the reduction of $FeCl_2^+$ to $FeCl_2$ and the formation of $Cl^-$ anions. The unreacted $Cl^-$ anions and $FeCl_4^-$ anions then coexist within the polymer chain due to Coulombic interactions. As can be seen in Fig. 3, the broad Cl peak of the doped polymer films can be deconvoluted into three distinct peaks at 197, 199, and 200 eV, which are attributable to both $FeCl_4^-$ and $FeCl_2$ species, $Cl^-$, and $FeCl_2^+$, respectively.[73–75] Hence, the proportion of dopants ionized by charge transfer to the conjugated polymer can be expressed as $\eta_d$, as calculated by eqn (2):

$$\eta_d = \frac{A^-}{A^0 + A^-} \quad (2)$$

where $A^0$ is the area of $FeCl_2^+$ peak and $A^-$ is the sum of areas from $Cl^-$ and $FeCl_2$ species peak. The estimated $\eta_d$ of the doped **P(Si–Si)**, **P(Si–O)**, and **P(Si–F)** films were 50.6, 70.6, and 59.0%,

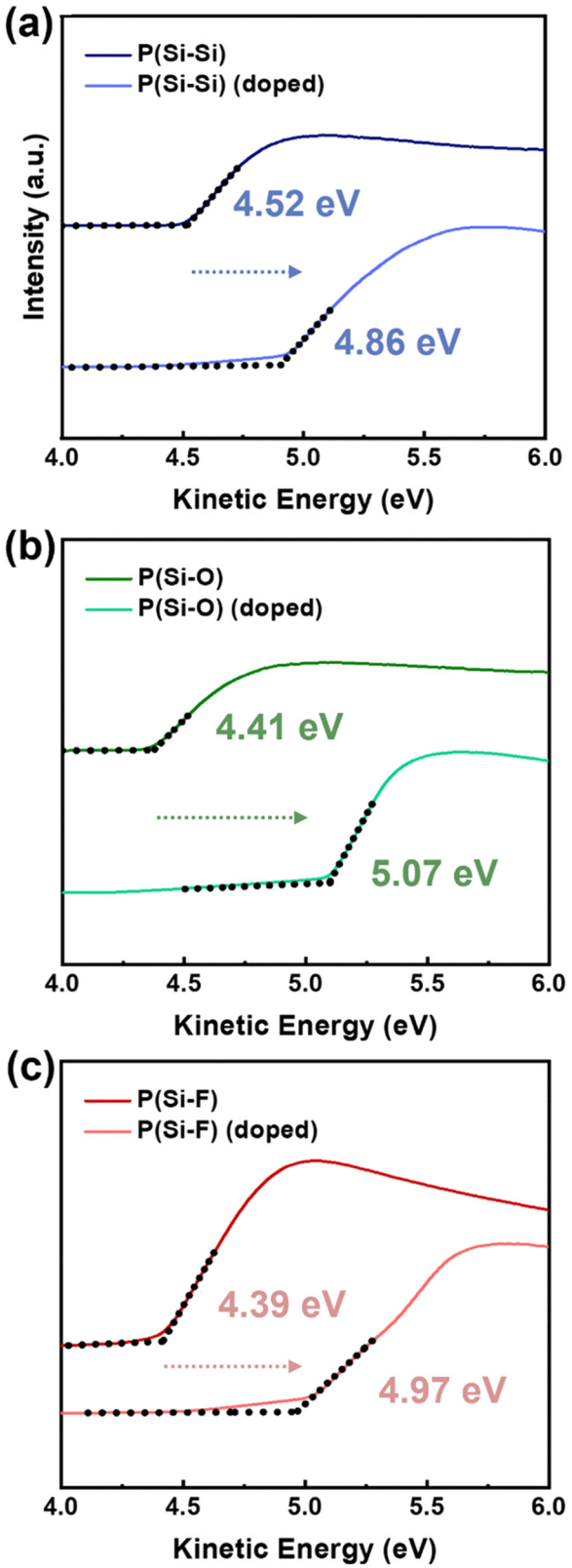


Fig. 2 UPS secondary electron cutoff (SECO) of undoped and $FeCl_3$-doped (a) **P(Si–Si)**, (b) **P(Si–O)**, and (c) **P(Si–F)** films.

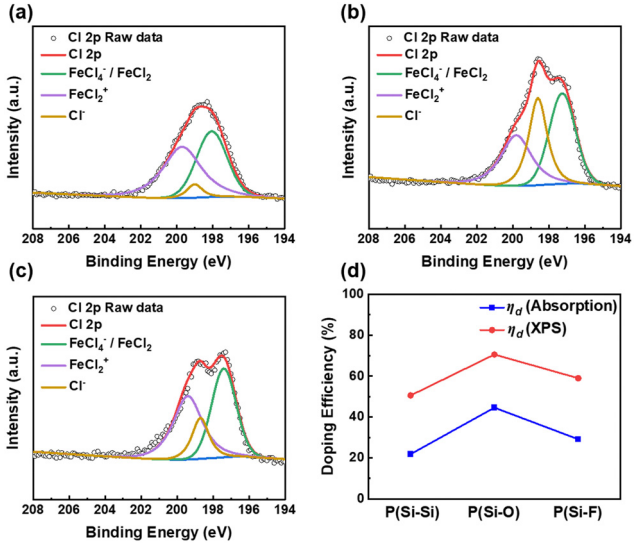


Fig. 3 The high solution Cl 2p XPS spectra of $FeCl_3$-doped (a) **P(Si–Si)**, (b) **P(Si–O)**, and (c) **P(Si–F)** film. (d) The doping efficiency of these three polymers doped by $FeCl_3$ calculated by absorption spectra and XPS.

respectively, showing a trend similar to the data obtained from the absorption spectra (Fig. 1). These results indicate that dopant molecules in **P(Si–O)** generate charge carriers more efficiently.

### 3.2. Morphological and microstructural characterization

AFM and GIWAXS were used to analyze the surface morphologies and changes in the orientation of the polymer films before and after the doping process. Fig. 4 display the height images of the three polymer films, which show fibrillar-like morphologies with root-mean-square roughness ($R_{rms}$) values of 3.7, 1.1, and 6.7 nm for **P(Si–Si)**, **P(Si–O)**, and **P(Si–F)**, respectively. The introduction of the polar oligoether side chains in **P(Si–O)** reduces aggregations, while $R_{rms}$ of **P(Si–F)** clearly increases. This is attributed to the strong aggregation from the semifluorinated side chains. The AFM images show notable morphological changes induced by $FeCl_3$ doping. After doping, some recognizable dot-like aggregates appeared on the surfaces, particularly for the doped **P(Si–Si)** and **P(Si–F)** films. A trend similar to the $R_{rms}$ of the doped films was observed, where the doped **P(Si–O)** film with the polar oligoether side chains shows the lowest $R_{rms}$, indicating better compatibility of $FeCl_3$ dopants with the oligoether side chains. This also indicates a favorable interaction between the oligoether side chains of **P(Si–O)** and the dopants, indicating relatively high doping efficiency. The appearance of the pronounced dot-like dopant aggregates on the **P(Si–Si)** and **P(Si–F)** films implies that their miscibilities with $FeCl_3$ dopants were poor owing to the low polar carbosilane and semifluorinated side chains and poor interactions with $FeCl_3$.[76] Additionally, to compare the miscibility differences of three polymer films, we measure the contact angle to calculate their surface energy (Fig. S2 and Table S2, ESI†). The results demonstrate that **P(Si–O)** modified with oligoether side chains exhibits a higher affinity for water. In contrast, **P(Si–F)** modified with semifluorinated side chains display more hydrophobic. The surface energy are 36.9, 28.5, and 38.3 mN $m^{-1}$ for **P(Si–Si)**, **P(Si–O)**, and **P(Si–F)**, respectively. Since the droplets of water or glycerol spread out into a flat shape on the $FeCl_3$ film, we can conclude that its surface energy is extremely low. Therefore, the surface energy difference between $FeCl_3$ and **P(Si–O)** is smaller compared to **P(Si–Si)** and **P(Si–F)**, suggesting that **P(Si–O)** has the best miscibility with $FeCl_3$.[77,78] This outcome is in agreement with the one obtained from AFM measurements.

The crystallographic characteristics of the pristine and doped polymer films were investigated using GIWAXS. Fig. 5 shows the two-dimensional (2D) GIWAXS patterns, which provide information about the packing ordering, orientation, and spacing, and the corresponding crystallographic parameters are summarized in Table 1. As shown in Fig. 5(a) and (b), the pristine **P(Si–Si)** and **P(Si–O)** films exhibit three scattering peaks arising from the ($h$00) reflection in the out-of-plane direction and the (010) reflection in the in-plane direction, being assignable to the lamellar and π–π stacking, demonstrating the crystalline microstructures with a predominant edge-on population with respect to the substrate. However, the asymmetric side chains on **P(Si–O)** caused a decrease in the relative degree of crystallinity, with a value of 0.69, using **P(Si–Si)** as a reference

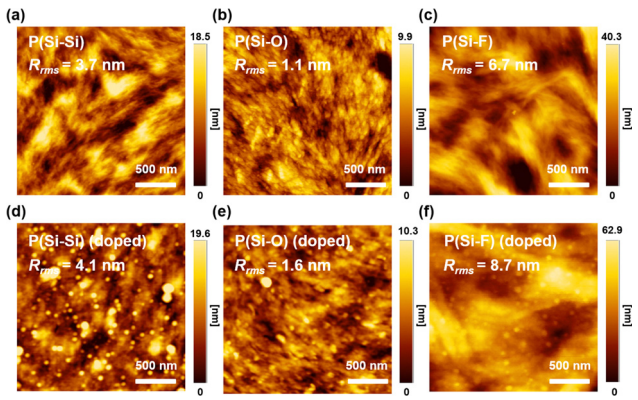


Fig. 4 AFM height images of (a–c) undoped polymer films and (d and e) $FeCl_3$-doped polymer films.

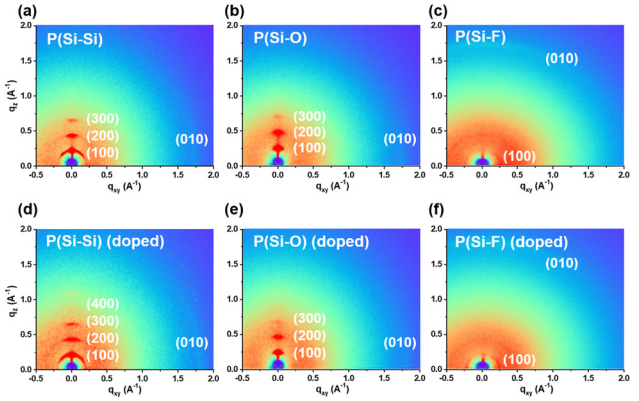


Fig. 5 2D GIWAXS patterns of (a–c) undoped polymer films and (d and e) $FeCl_3$-doped polymer films.

 

Table 1 Crystallographic parameters of undoped and $FeCl_3$-doped **P(Si–Si)**, **P(Si–O)**, and **(Si–F)** films

| Sample | Lamellar (100) spacing [Å] | π–π (010) spacing [Å] | rDoC | FWHM [$Å^{-1}$] | $L_c$ [Å] |
|---|---|---|---|---|---|
| **P(Si–Si)** | 26.8 | 3.6 | 1.00 | 0.033 | 190.4 |
| **P(Si–Si)** (doped) | 28.2 | 3.5 | 1.13 | 0.028 | 224.4 |
| **P(Si–O)** | 24.5 | 3.6 | 0.69 | 0.054 | 116.4 |
| **P(Si–O)** (doped) | 27.3 | 3.5 | 0.79 | 0.038 | 165.3 |
| **P(Si–F)** | 26.5 | 3.5 | 0.17 | N/A | N/A |
| **P(Si–F)** (doped) | 27.1 | 3.5 | 0.18 | N/A | N/A |

(1.00). In contrast, the (100) and (010) peaks of the pristine **P(Si–F)** film along $q_{xy}$ and $q_z$ directions were barely seen, with the rDoC being as low as 0.17. This indicates a disordered packing in the **P(Si–F)** sample. Moreover, the coherence lengths ($L_c$) calculated following the Scherrer equation from the full width at half maximum (FWHM) of the (100) diffraction peaks were 190.4 and 116.4 Å for **P(Si–Si)** and **P(Si–O)**, respectively, while that of **P(Si–F)** was negligible, indicating a shorter-range ordering for the asymmetric side chain substituents. After doping with $FeCl_3$, the edge-on structure was not affected, but the lamellar (100) spacing of the doped **P(Si–Si)** and **P(Si–O)** films increased, while the π–π stacking spacing decreased. This indicates that the conjugated polymers were oxidized by the transfer of electrons from the polymers to $FeCl_3$ *via* p-doing with the Coulombic attraction between the positively charged polymer backbones and the neighboring electron-rich π-moieties resulted in the intercalation of the dopants in the side chain regions of **P(Si–Si)** and **P(Si–O)**, simultaneously causing an expansion in the lamellar stacking and closer packing of polymer backbones.[34] The relatively higher rDoC, lower FWHM, and higher $L_c$ of the doped **P(Si–Si)** and **P(Si–O)** films indicate a more ordered crystalline structure that may facilitate the charge transport. The expansion in the lamellar spacing of doped **P(Si–O)** was greater than that of doped **P(Si–Si)** since more dopants were inserted in the polar oligoether side chains of **P(Si–O)** owing to the stronger intermolecular interaction. As a result of the low interaction between $FeCl_3$ and the semifluorinated side chains, the doped **P(Si–F)** films showed a slight change in the *d*-spacing when compared with the other two samples. Despite the less-ordered molecular packing, the bimodal face-on/edge-on orientation of **P(Si–F)** prefers to provide accommodation space for $FeCl_3$ dopants.[59] This suggests that **P(Si–F)** is more effective at doping than **P(Si–Si)** due to its lower crystallinity and bimodal orientation. However, the doping efficiency may be limited by the poor miscibility observed in the semifluorinated side chain regions, as shown by AFM images and contact angle measurements. In comparison to **P(Si–O)**, this could significantly impact the overall doping efficiency.

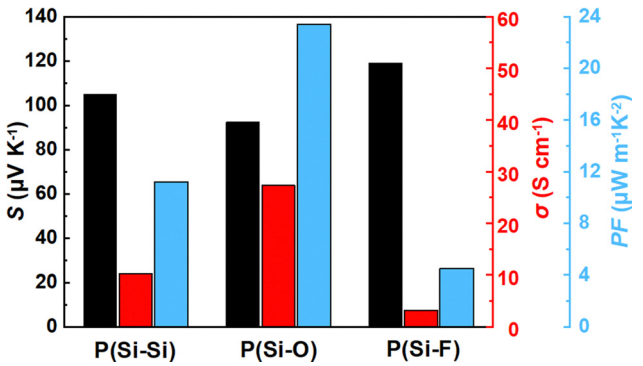


Fig. 6 Thermoelectric properties (*S*, σ, and PF) of $FeCl_3$-doped **P(Si–Si)**, **P(Si–O)**, and **P(Si–F)** films.

### 3.3. Thermoelectric properties

We carefully evaluated the thermoelectric properties of the $FeCl_3$-doped conjugated polymer films (Fig. 6 and Table 2) in terms of conductivity (σ), Seebeck coefficient (*S*), and power factor (PF), and all the thermoelectric parameters were measured in a vacuum chamber under a helium atmosphere to avoid temperature fluctuation and oxygen and moisture dedoping. It should be noted that the three pristine polymer samples exhibited poor σ, and thus the *S* could not be measured. As shown in Fig. 6, the doped **P(Si–Si)**, **P(Si–O)**, and **P(Si–F)** exhibited maximum σ of 10.2, 27.3, and 3.2 S $cm^{-1}$, respectively. This result indicates that the dominant factor in σ optimization correlates with doping efficiency. The $FeCl_3$-doped **P(Si–O)** film had the maximal σ, which is 2.7 × higher than that of **P(Si–Si)**. This increment in σ indicates the efficient doping effect of **P(Si–O)**, as already inferred from the relative strength of the intrinsic polymer absorption peak from the UV-vis-NIR spectra (Fig. 1(b)). This is also consistent with the improved morphologies of the **P(Si–O)** film after doping with $FeCl_3$, as confirmed by the AFM images (Fig. 4(e)), where the oligoether side chain had a favorable interaction with dopants and contributed to good miscibility between the dopant and the host polymer. The one-order of magnitude reduction for the **P(Si–F)** sample was due to the low crystalline and disordered structures and disrupted morphology previously mentioned; these factors may hinder the migration path of carriers. The conductive atomic force microscopy (C-AFM) measurements also provide the morphological information of conductive pathways within the conjugated polymer films

Table 2 Thermoelectric parameters of **P(Si–Si)**, **P(Si–O)**, and **P(Si–F)** films doped by $FeCl_3$

| Sample | μ [$cm^2$ $V^{-1}$ $s^{-1}$] | *n* [$cm^{-3}$] | σ [S $cm^{-1}$] | *S* [μV $K^{-1}$] | PF [μW $m^{-1}$ $K^{-2}$] |
|---|---|---|---|---|---|
| **P(Si–Si)** | 2.0 | $3.1 \times 10^{19}$ | 10.2 | 104.9 | 11.2 |
| **P(Si–O)** | 2.1 | $7.9 \times 10^{19}$ | 27.3 | 92.5 | 23.4 |
| **P(Si–F)** | 0.8 | $2.5 \times 10^{19}$ | 3.2 | 119.1 | 4.5 |

generated by the $FeCl_3$ doping process. Fig. S5(d)–(f) (ESI†) show the intermapping of the current distribution of the doped polymer films. It was found that the migration of the generated charge carrier from the doped **P(Si–O)** film current signals can be significantly delocalized across the entire film region, which again is consistent with the increased doping efficiency previously obtained. However, the current signals in the doped **P(Si–F)** film were only localized in a limited region together with the strongly aggregated region, suggesting that the conductive pathways associated with charge transport decreased.[79] The charge transport property can be quantitatively verified using mobility ($\mu$) results extracted from Hall measurement. The $\mu$ value of **P(Si–O)** increased up to 2.15 $cm^2\ V^{-1}\ s^{-1}$, demonstrating the proportional relationship between $\mu$ and $\sigma$. The positive $S$ values of all three doped polymers confirm the predominant p-doping characteristic. As shown in Fig. 6, the $S$ values of doped **P(Si–Si)**, **P(Si–O)**, and **P(Si–F)** were determined to be 104.9, 92.5, and 119.1 $\mu V\ K^{-1}$, respectively. Using the Hall effect measurement, we discovered that $S$ is inversely proportional to the carrier concentration ($n$), which also has an opposite direction relationship with $\sigma$. These results revealed $n$ values of 3.1, 7.9, and 2.5 $\times$ $10^{19}$ $cm^{-3}$ for **P(Si–Si)**, **P(Si–O)**, and **P(Si–F)**, respectively. **P(Si–O)** exhibited smaller $S$ values than the other two samples, indicating a higher $n$; this is consistent with the absorption spectra results (Fig. 1(b)). $FeCl_3$-doped **P(Si–O)** had the highest PF, reaching 23.4 $\mu W\ m^{-1}\ K^{-2}$. The optimized PF values for doped **P(Si–Si)** and **P(Si–F)** were 11.2 and 4.5 $\mu W\ m^{-1}\ K^{-2}$, respectively. The superior PF value of **P(Si–O)** to those of the other two polymers is attributable to the increased $\sigma$ without much loss in $S$. Collectively, the improved crystalline film morphologies of conjugated polymer films rather than the change in $n$ can significantly influence the $\sigma$ and thermoelectric properties owing to the optimal affinity between the dopant and polymer.

To better clarify the effect of side chain substitutions on charge transport physics of doped polymer film, we performed the $\sigma$ measurement while varying the sample temperatures from 303 to 323 K, where these temperature ranges were selected to avoid interference from the thermally induced dedoping process. For the doped films, the $\sigma$ increases as the temperature increase, indicating a correlation between the activation energy ($E_a$) and the energy barrier for charge transport can be expressed as eqn (3):

$$\sigma = \sigma_{max} \exp\left(\frac{-E_a}{k_B T}\right) \quad (3)$$

where $\sigma_{max}$ is the maximum $\sigma$ at 323 K and $k_B$ is the Boltzmann constant. As shown in Fig. 7, these three films were well-fitted with $E_a$ = 166, 87, and 396 meV for **P(Si–Si)**, **P(Si–O)**, and **P(Si–F)**, respectively. The $E_a$ of the $FeCl_3$-doped **P(Si–O)** film was lower than that of **P(Si–Si)** and **P(Si–F)**, indicating a reduction in the transport barrier between the intercrystalline domains due to the higher $\sigma$ of the former film. Moreover, the significantly higher $E_a$ of **P(Si–F)** results from the perturbed morphologies due to the self-aggregation of dopants. Thus, the high $\sigma$ and low $E_a$ of the **P(Si–O)** film can be the cause of the high doping efficiency and efficient charge transport path from the doped polymer structure.

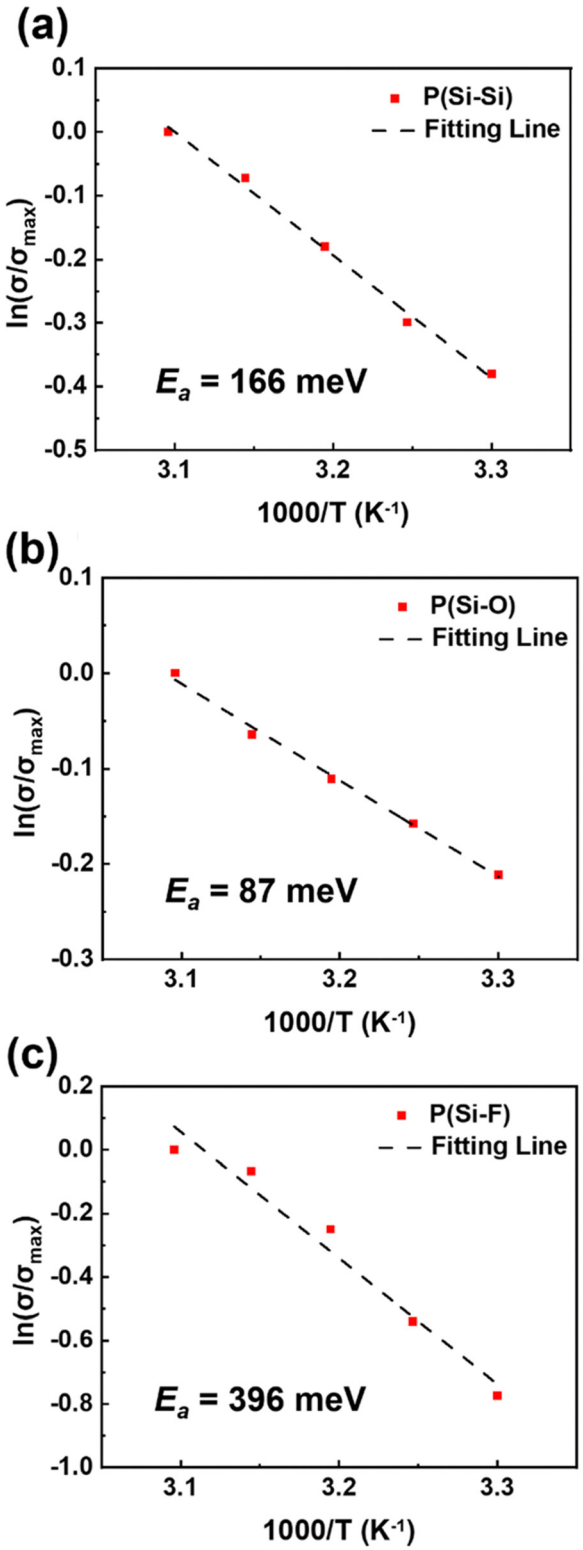


Fig. 7 Temperature-dependent $\sigma$ of $FeCl_3$-doped (a) **P(Si–Si)**, (b) **P(Si–O)**, and (c) **P(Si–F)** films. All doped polymer films were immersed in a 3 mg $mL^{-1}$ $FeCl_3$ solution for 3 min.

To sum up, we obtained a respectable thermoelectric PF of 23.4 $\mu W\ m^{-1}\ K^{-2}$ using the molecular design from asymmetric and oligoether side chains of IID-based donor–acceptor

 

conjugated copolymers. We devised a design strategy, which takes advantage of the high electrical conductivity and mobility, close π–π stacking, and high crystallinity of **P(Si–O)**, to achieve efficient charge transport and high doping miscibility in $FeCl_3$-doped donor–accepter conjugated polymers. Our analysis, which included AFM and contact angle measurements, has shown that hydrophilic side chain groups contribute to better miscibility with dopants. UV-vis-NIR spectroscopy, XPS, and UPS have confirmed that polymers with hydrophilic side chain groups lead to the highest doping efficiency and doping level after doping, resulting in the highest carrier concentration for **P(Si–O)** among the three polymers. GIWAXS analysis revealed that **P(Si–O)** maintains good polymer alignment, ensuring good mobility, and exhibits the highest electrical conductivity and a decent Seebeck coefficient, leading to the best thermoelectric performance. In contrast, modification with hydrophobic side chain groups (**P(Si–F)**) results in poor conductivity due to poor polymer alignment, which hinders carrier transport, despite having a higher doping efficiency from the higher proportion of amorphous regions. Furthermore, Fig. S6 (ESI†) compares the relationship between the $\sigma$, $S$, and PF of the previously reported $FeCl_3$-doped donor–acceptors conjugated polymers. Our IID-based donor–acceptor system can produce the typical $\sigma$–$S$ trade-off relationship under specific doping conditions. For a substantially higher $\sigma$, **P(Si–O)** exhibited a slightly lower $S$ than the other two samples. This is tentatively attributed to their high doping concentration. Our study has revealed that the $S$ values ($\sim$100 μV K$^{-1}$) of the three polymer films are more competitive than those of other samples. However, the $\sigma$ values were not as high as 100 S cm$^{-1}$. We believe that the further increased doping level (carrier concentration) should be applied instead of immersion in the $FeCl_3$ doping solution. Various doping methods, such as sequential twice doping,[37] vapor phase doping,[51] and incremental concentration doping,[53] as well as enhanced ordered conductive domains by high-temperature rubbing.[54] We will continue to focus on molecular design, specifically on polymer backbone structure and side chain engineering, with the goal of facilitating dopant diffusion into polymer chains. This will ultimately lead to enhanced doping efficiency and increased conductivity and PF in thermoelectric polymers. Additionally, our research efforts will also focus on the application of thermoelectric polymers in wearable devices that can efficiently generate electricity from body heat.

## 4. Conclusions

In conclusion, three IID-based donor–acceptor polymers with various side chain substituents, including two carbosilanes, carbosilane/oligoether, and carbosilane/semifluorinated side chain on both sides, were used to investigate the effect of side chain polarity on the thermoelectric properties of doped conjugated polymers. By inducing asymmetric and polar side chains, the polymer can create spacer domains to facilitate dopant diffusion into the side chain of polymers, further enhancing the doping efficiency. In this situation, we discovered that the hydrophilic oligoether side chain has a significant positive impact on microstructure and energetics. This modification is in turn detrimental to properties important in the thermoelectric device. Thus, **P(Si–O)** allows for favorable interaction with the $FeCl_3$ dopant, enhancing the doping efficiency and efficient charge transport while maintaining ordered thin film structural organization. Among these polymers, the **P(Si–O)** films doped with $FeCl_3$ exhibited the best thermoelectric performance, achieving the highest PF value. Our findings demonstrate the importance of miscibility between the dopant and host polymer as well as molecular ordering for achieving high $\sigma$ in doped conjugated polymer films. Our findings also provide insight into the molecular design of side chain engineering for excellent thermoelectric performance.

## Conflicts of interest

There are no conflicts to declare.

## Acknowledgements

The authors acknowledge the financial support from the 2030 Cross-Generation Young Scholars Program by the National Science and Technology Council (NSTC) in Taiwan, under grant 111-2628-E-002-014 and 112-2628-E-002-013. Y.-C. L. thanks the financial support from the NSTC in Taiwan (111-2222-E-006-020-MY2). The authors also thank Beamline TLS 13A1/17A1 and TPS 25A at the National Synchrotron Radiation Research Center (NSRRC) of Taiwan for providing beamtime.

## References

1 Z. Miao, X. Meng and L. Liu, *J. Power Sources*, 2022, **541**, 231699.
2 B. Qin, D. Wang, X. Liu, Y. Qin, J. F. Dong, J. Luo, J. W. Li, W. Liu, G. Tan, X. Tang and J. F. Li, *Science*, 2021, **373**, 556–561.
3 J. J. Yoo, G. Seo, M. R. Chua, T. G. Park, Y. Lu, F. Rotermund, Y. K. Kim, C. S. Moon, N. J. Jeon, J. P. Correa-Baena, V. Bulovic, S. S. Shin, M. G. Bawendi and J. Seo, *Nature*, 2021, **590**, 587–593.
4 D. Bao, J. Chen, Y. Yu, W. Liu, L. Huang, G. Han, J. Tang, D. Zhou, L. Yang and Z.-G. Chen, *Chem. Eng. J.*, 2020, **388**, 124295.
5 M. N. Hasan, M. Nafea, N. Nayan and M. S. Mohamed Ali, *Adv. Mater. Technol.*, 2021, **7**, 2101203.
6 X. L. Shi, J. Zou and Z. G. Chen, *Chem. Rev.*, 2020, **120**, 7399–7515.
7 M. Mukherjee, A. Srivastava and A. K. Singh, *J. Mater. Chem. C*, 2022, **10**, 12524–12555.
8 Z. Fan and J. Ouyang, *Adv. Electron. Mater.*, 2019, **5**, 1800769.
9 M. Goel and M. Thelakkat, *Macromolecules*, 2020, **53**, 3632–3642.
10 N. Nandihalli, C.-J. Liu and T. Mori, *Nano Energy*, 2020, **78**, 105186.
11 F. Zhang and C.-a Di, *Chem. Mater.*, 2020, **32**, 2688–2702.

12 W. Zhao, J. Ding, Y. Zou, C. A. Di and D. Zhu, *Chem. Soc. Rev.*, 2020, **49**, 7210–7228.
13 M. Massetti, F. Jiao, A. J. Ferguson, D. Zhao, K. Wijeratne, A. Wurger, J. L. Blackburn, X. Crispin and S. Fabiano, *Chem. Rev.*, 2021, **121**, 12465–12547.
14 T. L. D. Tam and J. Xu, *J. Mater. Chem. A*, 2021, **9**, 5149–5163.
15 S. Xu, X.-L. Shi, M. Dargusch, C. Di, J. Zou and Z.-G. Chen, *Prog. Mater. Sci.*, 2021, **121**, 100840.
16 L. Zhang, X.-L. Shi, Y.-L. Yang and Z.-G. Chen, *Mater. Today*, 2021, **46**, 62–108.
17 L. Deng, Y. Liu, Y. Zhang, S. Wang and P. Gao, *Adv. Funct. Mater.*, 2022, **33**, 2210770.
18 A. D. Scaccabarozzi, A. Basu, F. Anies, J. Liu, O. Zapata-Arteaga, R. Warren, Y. Firdaus, M. I. Nugraha, Y. Lin, M. Campoy-Quiles, N. Koch, C. Muller, L. Tsetseris, M. Heeney and T. D. Anthopoulos, *Chem. Rev.*, 2022, **122**, 4420–4492.
19 J. Tang, Y.-H. Pai and Z. Liang, *ACS Energy Lett.*, 2022, **7**, 4299–4324.
20 A. Tripathi, Y. Lee, S. Lee and H. Y. Woo, *J. Mater. Chem. C*, 2022, **10**, 6114–6140.
21 S. Wang, G. Zuo, J. Kim and H. Sirringhaus, *Prog. Polym. Sci.*, 2022, **129**, 101548.
22 D. Zhou, H. Zhang, H. Zheng, Z. Xu, H. Xu, H. Guo, P. Li, Y. Tong, B. Hu and L. Chen, *Small*, 2022, **18**, 2200679.
23 T. Cao, X.-L. Shi, J. Zou and Z.-G. Chen, *Microstruct.*, 2021, **1**, 2021007.
24 W.-Y. Chen, X.-L. Shi, J. Zou and Z.-G. Chen, *Mater. Sci. Eng., R*, 2022, **151**, 100700.
25 X. Liu, X.-L. Shi, L. Zhang, W.-D. Liu, Y. Yang and Z.-G. Chen, *J. Mater. Sci. Technol.*, 2023, **132**, 81–89.
26 A. Liang, X. Zhou, W. Zhou, T. Wan, L. Wang, C. Pan and L. Wang, *Macromol. Rapid Commun.*, 2017, **38**, 1600817.
27 Y. Song, J. Ding, X. Dai, C. Li, C.-A. Di and D. Zhang, *ACS Mater. Lett.*, 2022, **4**, 521–527.
28 J. Wu, X. Yin, F. Yang, S. Wang, Y. Liu, X. Mao, X. Nie, S. Yang, C. Gao and L. Wang, *Chem. Eng. J.*, 2022, **429**, 132354.
29 D. X. Xie, T. C. Liu, J. Xiao, J. K. Fang, C. J. Pan and G. Shao, *Molecules*, 2021, **26**, 963–972.
30 S. E. Yoon, S. J. Shin, S. Y. Lee, G. G. Jeon, H. Kang, H. Seo, J. Zheng and J. H. Kim, *ACS Appl. Polym. Mater.*, 2020, **2**, 2729–2735.
31 H. Zhou, C. Gao, T. Liu, C. Pan and L. Wang, *J. Mater. Chem. C*, 2020, **8**, 7096–7103.
32 J. Ding, Z. Liu, W. Zhao, W. Jin, L. Xiang, Z. Wang, Y. Zeng, Y. Zou, F. Zhang, Y. Yi, Y. Diao, C. R. McNeill, C. A. Di, D. Zhang and D. Zhu, *Angew. Chem., Int. Ed.*, 2019, **58**, 18994–18999.
33 X. Zhou, C. Pan, C. Gao, A. Shinohara, X. Yin, L. Wang, Y. Li, Q. Jiang, C. Yang and L. Wang, *J. Mater. Chem. A*, 2019, **7**, 10422–10430.
34 F. Zhong, X. Yin, Z. Chen, C. Gao and L. Wang, *ACS Appl. Mater. Interfaces*, 2020, **12**, 26276–26285.
35 Y. Hu, Y. Gao, P. Li, X. Gao and Z. Liu, *J. Polym. Sci.*, 2021, **60**, 1002–1012.
36 X. Y. Wang, Y. Liu, Z. Y. Wang, Y. Lu, Z. F. Yao, Y. F. Ding, Z. D. Yu, J. Y. Wang and J. Pei, *J. Polym. Sci.*, 2021, **60**, 538–547.
37 H. Chai, Z. Xu, H. Li, F. Zhong, S. Bai and L. Chen, *ACS Appl. Electron. Mater.*, 2022, **4**, 4947–4954.
38 L. Chen, W. Wang, S. Xiao and X. Tang, *Chin. Phys. B*, 2022, **31**, 028507.
39 T. S. Lee, S. B. Lee, D.-Y. Choi, E. H. Suh, T. K. An, Y. J. Jeong, J. Jang and Y.-H. Kim, *Macromol. Res.*, 2022, **29**, 887–894.
40 J. Tang, J. Ji, R. Chen, Y. Yan, Y. Zhao and Z. Liang, *Adv. Sci.*, 2022, **9**, 2103646.
41 H. Li, J. Song, J. Xiao, L. Wu, H. E. Katz and L. Chen, *Adv. Funct. Mater.*, 2020, **30**, 2004378.
42 Y. Karpov, T. Erdmann, I. Raguzin, M. Al-Hussein, M. Binner, U. Lappan, M. Stamm, K. L. Gerasimov, T. Beryozkina, V. Bakulev, D. V. Anokhin, D. A. Ivanov, F. Gunther, S. Gemming, G. Seifert, B. Voit, R. Di Pietro and A. Kiriy, *Adv. Mater.*, 2016, **28**, 6003–6010.
43 V. Vijayakumar, E. Zaborova, L. Biniek, H. Zeng, L. Herrmann, A. Carvalho, O. Boyron, N. Leclerc and M. Brinkmann, *ACS Appl. Mater. Interfaces*, 2019, **11**, 4942–4953.
44 P. Durand, H. Zeng, T. Biskup, V. Vijayakumar, V. Untilova, C. Kiefer, B. Heinrich, L. Herrmann, M. Brinkmann and N. Leclerc, *Adv. Energy Mater.*, 2021, **12**, 2103049.
45 P. A. Finn, I. E. Jacobs, J. Armitage, R. Wu, B. D. Paulsen, M. Freeley, M. Palma, J. Rivnay, H. Sirringhaus and C. B. Nielsen, *J. Mater. Chem. C*, 2020, **8**, 16216–16223.
46 R. Kroon, D. Kiefer, D. Stegerer, L. Yu, M. Sommer and C. Muller, *Adv. Mater.*, 2017, **29**, 170093.
47 A. Tripathi, Y. Ko, M. Kim, Y. Lee, S. Lee, J. Park, Y.-W. Kwon, J. Kwak and H. Y. Woo, *Macromolecules*, 2020, **53**, 7063–7072.
48 H. Zeng, P. Durand, S. Guchait, L. Herrmann, C. Kiefer, N. Leclerc and M. Brinkmann, *J. Mater. Chem. C*, 2022, **10**, 15883–15896.
49 T. Ma, B. X. Dong, J. W. Onorato, J. Niklas, O. Poluektov, C. K. Luscombe and S. N. Patel, *J. Polym. Sci.*, 2021, **59**, 2797–2808.
50 J. Min Han, S. Eun Yoon, K. Hyun Jung, O. Bae, D. Kim, U. Kim, H. Seo, F. Sunjoo Kim, K. Chul Kim, J. H. Kim and B.-G. Kim, *Chem. Eng. J.*, 2022, **431**, 133779.
51 J. Min, D. Kim, S. G. Han, C. Park, H. Lim, W. Sung and K. Cho, *Adv. Electron. Mater.*, 2021, **8**, 2101142.
52 E. H. Suh, M. K. Jeong, K. Lee, W. Jeong, J. Jang and I. H. Jung, *Int. J. Energy Res.*, 2021, **45**, 21540–21551.
53 V. Untilova, H. Zeng, P. Durand, L. Herrmann, N. Leclerc and M. Brinkmann, *Macromolecules*, 2021, **54**, 6073–6084.
54 V. Untilova, T. Biskup, L. Biniek, V. Vijayakumar and M. Brinkmann, *Macromolecules*, 2020, **53**, 2441–2453.
55 W. Xing, S. Wu, Y. Liang, Y. Sun, Y. Zou, L. Liu, W. Xu and D. Zhu, *ACS Appl. Mater. Interfaces*, 2020, **12**, 29540–29548.
56 S. E. Yoon, B. Kim, S. Y. Chun, S. Y. Lee, D. Jeon, M. Kim, S. Lee, B. E. Seo, K. S. Choi, F. S. Kim, T. Kim, H. Seo, K. Kwak, J. H. Kim and B. Kim, *Adv. Funct. Mater.*, 2022, **32**, 2202929.
57 C. K. Mai, R. A. Schlitz, G. M. Su, D. Spitzer, X. Wang, S. L. Fronk, D. G. Cahill, M. L. Chabinyc and G. C. Bazan, *J. Am. Chem. Soc.*, 2014, **136**, 13478–13481.

 

58 Y. Wang, M. Nakano, T. Michinobu, Y. Kiyota, T. Mori and K. Takimiya, *Macromolecules*, 2017, **50**, 857–864.
59 Y. Wang and K. Takimiya, *Adv. Mater.*, 2020, **32**, 2002060.
60 W. Choi, S. Kim, S. Lee, C. Jung, A. Tripathi, Y. Lee, H. Y. Woo and H. Lee, *Small Methods*, 2023, **7**, 2201145.
61 D. Kiefer, A. Giovannitti, H. Sun, T. Biskup, A. Hofmann, M. Koopmans, C. Cendra, S. Weber, L. J. Anton Koster, E. Olsson, J. Rivnay, S. Fabiano, I. McCulloch and C. Muller, *ACS Energy Lett.*, 2018, **3**, 278–285.
62 J. Liu, L. Qiu, R. Alessandri, X. Qiu, G. Portale, J. Dong, W. Talsma, G. Ye, A. A. Sengrian, P. C. T. Souza, M. A. Loi, R. C. Chiechi, S. J. Marrink, J. C. Hummelen and L. J. A. Koster, *Adv. Mater.*, 2018, **30**, 1704630.
63 J. Liu, L. Qiu, G. Portale, M. Koopmans, G. Ten Brink, J. C. Hummelen and L. J. A. Koster, *Adv. Mater.*, 2017, **29**, 1701641.
64 J. Liu, G. Ye, H. G. O. Potgieser, M. Koopmans, S. Sami, M. I. Nugraha, D. R. Villalva, H. Sun, J. Dong, X. Yang, X. Qiu, C. Yao, G. Portale, S. Fabiano, T. D. Anthopoulos, D. Baran, R. W. A. Havenith, R. C. Chiechi and L. J. A. Koster, *Adv. Mater.*, 2021, **33**, 2006694.
65 L. Qiu, J. Liu, R. Alessandri, X. Qiu, M. Koopmans, R. W. A. Havenith, S. J. Marrink, R. C. Chiechi, L. J. Anton Koster and J. C. Hummelen, *J. Mater. Chem. A*, 2017, **5**, 21234–21241.
66 Y. Shi, J. Li, H. Sun, Y. Li, Y. Wang, Z. Wu, S. Y. Jeong, H. Y. Woo, S. Fabiano and X. Guo, *Angew. Chem., Int. Ed.*, 2022, **61**, 202214192.
67 Y.-h Shin, H. Komber, D. Caiola, M. Cassinelli, H. Sun, D. Stegerer, M. Schreiter, K. Horatz, F. Lissel, X. Jiao, C. R. McNeill, S. Cimò, C. Bertarelli, S. Fabiano, M. Caironi and M. Sommer, *Macromolecules*, 2020, **53**, 5158–5168.
68 K. Takagi, H. Yano, H. Ito and N. Kishi, *Polymer*, 2019, **181**, 121787.
69 G. Ye, J. Liu, X. Qiu, S. Stater, L. Qiu, Y. Liu, X. Yang, R. Hildner, L. J. A. Koster and R. C. Chiechi, *Macromolecules*, 2021, **54**, 3886–3896.
70 Y. C. Lin, F. H. Chen, Y. C. Chiang, C. C. Chueh and W. C. Chen, *ACS Appl. Mater. Interfaces*, 2019, **11**, 34158–34170.
71 H.-C. Yen, Y.-C. Lin and W.-C. Chen, *Macromolecules*, 2021, **54**, 1665–1676.
72 T. Lei, J. Y. Wang and J. Pei, *Acc. Chem. Res.*, 2014, **47**, 1117–1126.
73 Y. H. Kang, S.-J. Ko, M.-H. Lee, Y. K. Lee, B. J. Kim and S. Y. Cho, *Nano Energy*, 2021, **82**, 105681.
74 M. V. Russo, G. Polzonetti and A. Furlani, *Synth. Met.*, 1991, **39**, 291–301.
75 A. Furlani, M. V. Russo, G. Polzonetti, K. Martin, H. H. Wang and J. R. Ferraro, *Appl. Spectrosc.*, 1990, **44**, 331–334.
76 J. G. Riess, *Artif. Cells, Blood Substitutes, Biotechnol.*, 2005, **33**, 47–63.
77 J. Guo, K. Hu, B. Qiu, J. Zhang, D. Yang, L. Zhou, S. Li, L. Meng, Z. Zhang and Y. Li, *ACS Appl. Mater. Interfaces*, 2021, **13**, 36033–36043.
78 D. Rosas Villalva, S. Singh, L. A. Galuska, A. Sharma, J. Han, J. Liu, M. A. Haque, S. Jang, A. H. Emwas, L. J. A. Koster, X. Gu, B. C. Schroeder and D. Baran, *Mater. Horiz.*, 2022, **9**, 500–508.
79 C. Y. Yang, W. L. Jin, J. Wang, Y. F. Ding, S. Nong, K. Shi, Y. Lu, Y. Z. Dai, F. D. Zhuang, T. Lei, C. A. Di, D. Zhu, J. Y. Wang and J. Pei, *Adv. Mater.*, 2018, **30**, 1802850.